

Plastic deformation of Fe-Al polycrystals strengthened with Zr-containing Laves phases

Part II. Mechanical properties

A. Wasilkowska^{a,1}, M. Bartsch^a, F. Stein^b, M. Palm^b,
G. Sauthoff^b, U. Messerschmidt^{a,*}

^a Max-Planck-Institut für Mikrostrukturphysik, Weinberg 2, D-06120 Halle/Saale, Germany

^b Max-Planck-Institut für Eisenforschung, Max-Planck-Str.1, D-40074 Düsseldorf, Germany

Received 22 August 2003; received in revised form 21 January 2004

Abstract

Fe-10 at.% Al-2.5 at.% Zr and Fe-20 at.% Al-2.5 at.% Zr alloys were deformed between room temperature and 700 °C. The materials show a flow stress plateau at about 300 MPa up to 600 °C for the material with 10 at.% Al and above 600 MPa up to 400 °C for the alloy with 20% Al. The high flow stresses compared to Fe-Al reference materials are partly due to the addition of Zr. The strain rate sensitivity of the flow stress was measured by stress relaxation and strain rate cycling tests. It is low up to 400 °C and high between 450 and 600 °C, i.e. in the range of the flow stress decrease. The microstructures of the undeformed materials are described in Part I of this paper. Micrographs of the deformed specimens taken in a high-voltage electron microscope reveal that the deformation occurs mainly within the soft Fe-Al grains and in the Fe-Al component of the grain boundary eutectic. The deformation data are interpreted in terms of solution hardening from the Al solute, dynamic strain ageing due to the Cottrell effect of the same defects, the athermal stress component of elastic dislocation interactions, the Hall–Petch contribution from the grain size, and the strengthening effect of the grain boundary layers.

© 2004 Elsevier B.V. All rights reserved.

Keywords: Fe-Al-Zr; Laves phase strengthening; Plastic deformation; Dislocation structure; Deformation mechanisms

1. Introduction

The challenge to develop high-temperature materials with a good combination of strength and ductility has lead to a new class of structural materials: the Laves phase-strengthened intermetallics [1–3]. Within this class, the Triballoys which contain large volume fractions of the Mo(Co, Si)₂ Laves phase have excellent wear and corrosion resistance [1]. In Ti–Nb–Cr alloys, (Ti, Nb)Cr₂ particles precipitate resulting in a high strength together with acceptable room-temperature toughness. The particles break during deformation with crack arrest at the phase boundaries [2]. For directionally solidified NiAl-Ta alloys, the room

temperature toughness of two-phase alloys with off-eutectic composition was similar to that of polycrystalline NiAl even though the brittle Laves phase NiAlTa was present [3]. Alloying Fe-rich aluminides with up to 25 at.% Zr benefits from the precipitation of Zr(Fe,Al)₂ Laves phases [4,5]. These materials retain a high room-temperature strength up to around 400 °C [6]. In the present study, the deformation behaviour of ductile Fe-10Al-2.5Zr and Fe-20Al-2.5Zr alloys (numbers indicate at.%) strengthened with Zr(Fe,Al)₂ Laves phases has been studied in more detail also with respect to the strain rate sensitivity of the flow stress and the relation to changes in the microstructure. Both alloys contain about 20 vol.% of a eutectic containing the Laves phase, which is precipitated along the matrix grain boundaries. In addition, data for reference alloys Fe-10Al and Fe-20Al without Laves phase precipitates as well as for Fe-30Zr consisting mainly of the Laves phase are presented. Details of the starting structure of several Fe-Al-Zr alloys are described in Part I of this paper [7] and first results on plastic deformation in [8].

* Corresponding author. Tel.: +49 345 5582 927; fax: +49 345 5511223.

E-mail address: um@mpi-halle.de (U. Messerschmidt).

¹ Present address: TU München, Lehrstuhl für Materialwiss. und Mechanik, Boltzmannstr. 15, D-85748 Garching, Germany.

2. Experimental

In the following, the two Laves phase-strengthened alloys are called F10AZ and F20AZ and the reference alloys without Zr F10A and F20A. The composition and some structural data are listed in Table 1. The reference alloys have mainly columnar grains with a diameter of about 150 and 300 μm and up to several millimeters length. For the mechanical tests, samples of about 2 mm \times 2 mm \times 4 mm were cut from the ingots by electrical discharge machining and their faces were subsequently carefully polished. Compression experiments were carried out in a digitally controlled testing machine at temperatures between 23 and 700 $^{\circ}\text{C}$ in flowing argon at a basic strain rate of 10^{-4} s^{-1} . The engineering stress σ was measured versus the total engineering strain ε_t . The yield stress σ_y was determined by linear back extrapolation of the initial work-hardening range onto the elastic line. In order to study the strain rate sensitivity $r = \Delta\sigma/\Delta \ln \dot{\varepsilon}$, where $\dot{\varepsilon}$ is the plastic strain rate, usually a sequence of stress relaxation (R_n) and strain rate change (SRC) tests were performed during the deformation as shown in Fig. 1. Stress relaxation curves were plotted as $\ln(-\dot{\sigma})$ versus σ . The strain rate sensitivity is then given by the inverse slope of these curves as $r_{\text{rel}} = \Delta\sigma/\Delta \ln(-\dot{\sigma})$. In order to obtain information about changes of the microstructure during the relaxation tests, some “repeated” relaxation tests (R_{nr}) were performed, i.e. relaxation tests following an original relaxation and starting at a stress not exceeding that of the original relaxation. Thus, repeated relaxation tests are carried out before quasi-steady state deformation conditions are reached again. For SRC tests, two quantities of the strain rate sensitivity are determined as demonstrated in Fig. 1. The instantaneous strain rate sensitivity r_i is calculated from the maximum (instantaneous) stress increment $\Delta\sigma_i$ immediately after the strain rate change. Since the strain necessary to measure this quantity is small, structural changes during the change of the deformation conditions should also be small. Thus, this quantity may correspond to the strain rate sensitivity r_{rel} measured from stress relaxation tests, where little strain is consumed, too. In addition, the steady state strain rate sensitivity r_{ss} is obtained from the back-extrapolated stress increment $\Delta\sigma_{\text{ss}}$ of the quasi-steady state deformation after the strain rate change. The difference between r_i and r_{ss} characterizes structural changes caused by a change in the deformation conditions. Another measure of the strain rate sensitivity is the stress exponent m' of the strain rate, with $m' = d \ln \dot{\varepsilon} / d \ln \sigma$. It is related to r by $m' = \sigma / r$.

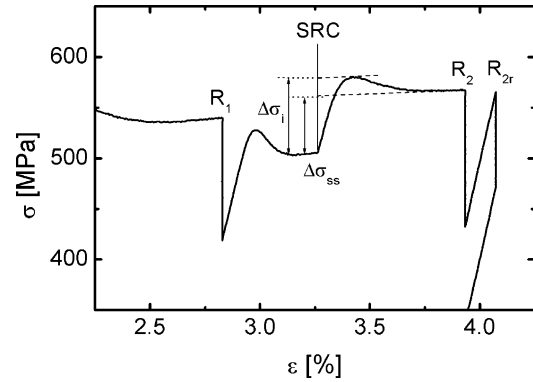


Fig. 1. Section of a stress–strain curve (flow stress σ vs. total strain ε_t) with stress relaxation tests (R_n), repeated relaxation test (R_{nr}) and strain rate cycling test (SRC). The stress increments $\Delta\sigma_i$ and $\Delta\sigma_{\text{ss}}$ are used to calculate the instantaneous and steady state strain rate sensitivities r_i and r_{ss} .

To study the deformation microstructures, specimens were deformed up to plastic strains of about 2.5–3% and then cooled under load. The surface of the deformed specimens was studied by scanning electron microscopy (SEM). Thin foils for transmission electron microscopy (TEM) were prepared normal to the compression axis by electrolytic jet polishing in 10% perchloric acid in ethanol and 7 g thiourea per 1000 cm^3 [9]. These samples were investigated in diffraction contrast in a high-voltage transmission electron microscope (HVTEM) operated at an acceleration voltage of 1 MV. Dislocation densities within the Fe–Al grains were measured from the number of intersections with a square grid. The foil thickness was estimated from extinction fringes on dislocations to be about 500 nm.

A few in situ heating experiments on deformed specimens have been performed in a heating stage inside the HVTEM to study the influence of heating cycles on the microstructure. The heating cycles were: 23 \rightarrow 370 \rightarrow 600 $^{\circ}\text{C}$, 23 \rightarrow 370 \rightarrow 490 \rightarrow 650 $^{\circ}\text{C}$, and 400 \rightarrow 23 $^{\circ}\text{C}$ over a total time of 5 h. Changes in the microstructure were recorded on video tape.

3. Results

3.1. Macroscopic deformation parameters

Fig. 2 presents a stress–strain curve of F10AZ at 340 $^{\circ}\text{C}$ with stress relaxation and strain rate change tests. It is typical also of other deformation conditions. The curve shows

Table 1
Characteristics of the two-phase materials (from [7])

Alloy	Composition (at%)			Phase structure	Structure parameters			
	Fe	Al	Zr		\bar{D} [μm]	f_{GB} [%]	S [mm^{-1}]	d [μm]
F10AZ	87.5	10	2.5	$\alpha\text{-Fe(Al)} + \text{Zr(Fe,Al)}_2$	28 ± 14	22	144	0.22
F20AZ	77.5	20	2.5	$\text{Fe-Al} + \text{Zr(Fe,Al)}_2$	20 ± 8	25	193	0.16

\bar{D} : grain size; f_{GB} : volume fraction and; S : mean surface area per volume (of grain boundary phase relates to both f_{GB} and S).

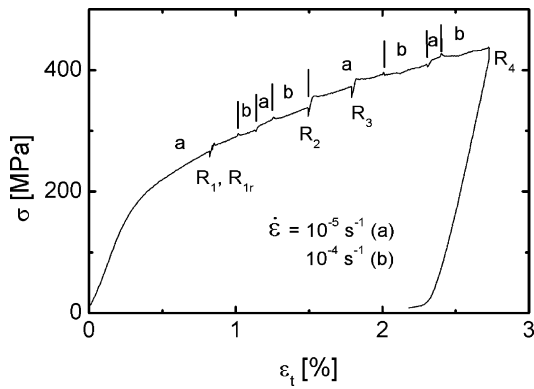


Fig. 2. Section of a stress–strain curve of F10AZ at 340°C including stress relaxation (R_n), repeated stress relaxation (R_{nr}) and strain rate cycling (SRC) tests between the strain rates of $\dot{\epsilon}_t = 10^{-5} \text{ s}^{-1}$ (a) and 10^{-4} s^{-1} (b).

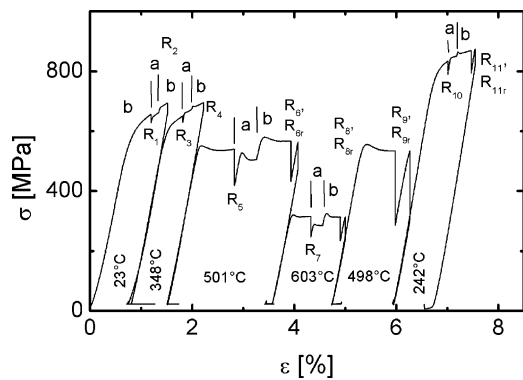


Fig. 3. Stress–strain curve of F20AZ at different temperatures and strain rates of $\dot{\epsilon}_t = 10^{-5} \text{ s}^{-1}$ (a) and 10^{-4} s^{-1} (b).

the transition between elastic and plastic deformation and a work-hardening stage with a decreasing work-hardening rate (parabolic hardening). In order to obtain strain rate sensitivity data from a limited number of experiments, some specimens were deformed successively at different temperatures, as shown in Fig. 3 for an F20AZ sample. The temperature dependence of the yield stress σ_y is plotted in Fig. 4.

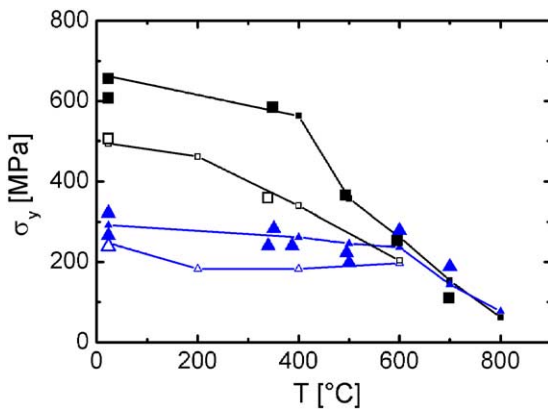


Fig. 4. Temperature dependence of the yield stress σ_y of F10A (open triangles), F10AZ (solid triangles), F20A (open squares), and F20AZ (solid squares). Small symbols: data from [6].

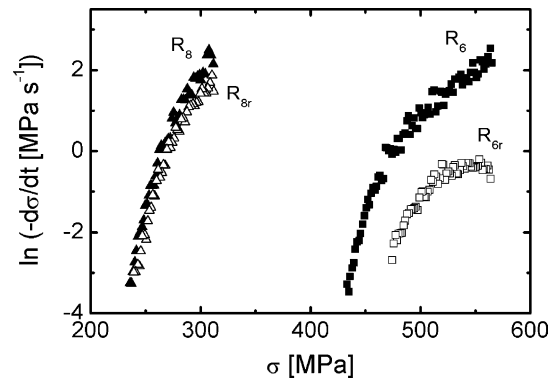


Fig. 5. Stress relaxation curves and repeated relaxation curves of the F20AZ specimen of Fig. 3 at 501°C (R_6 , R_{6r}) and at 603°C (R_8 , R_{8r}).

Only stress values of the initial loading are used. In addition to the present data (large symbols), 0.2% proof stresses are shown which have been determined previously [6] (small symbols). The data of the Laves phase-strengthened materials are compared with the reference materials without Zr, F10A and F20A. The reference material F10A exhibits an almost constant yield stress up to 600°C. The corresponding material containing Zr has a yield stress which is higher by a constant amount. Above 600°C, the yield stress shows a strong high-temperature decrease. The materials with the higher Al content show higher yield stresses but an earlier start of the high-temperature decrease.

Fig. 5 exhibits stress relaxation curves of F20AZ taken at about 500°C (R_6) and 600°C (R_8). The strain rate sensitivity r equals the inverse slope of these curves. Usually, r is measured at the beginning of the relaxation curves. Then, the values correspond to the state of the specimen just at the start of the relaxation test. The relaxation curves in Fig. 5 are bowed towards the stress axis. This is the usual curvature corresponding, e.g., to dislocations overcoming obstacles. At 600°C, the repeated relaxation curve (R_{6r}) is very close to the original one (R_6), indicating that either structural changes did not occur during the relaxation, or that they occurred fast so that the deformation always took place close to steady state. However, at 500°C, the relaxation rates, which are proportional to the current strain rates, are drastically lower in case of the repeated relaxation curve (R_{6r}) than those of the original relaxation curve. This suggests structural changes during the relaxation and is mostly connected with a yield point effect during further deformation with a transition into steady state conditions. The difference in the relaxation rates between original and repeated relaxation curves is generally low for F10AZ and for F20AZ at room temperature and above 600°C but increases up to a factor of 20 for F20AZ and F20A in the temperature interval between 350 and 500°C. Fig. 6 presents a relaxation curve of F10AZ taken at 500°C. In this case, the curve is bent away from the stress axis, which may be denoted by a relaxation curve with an inverse curvature or a curve with two stages, a steep initial stage with a low r value at high

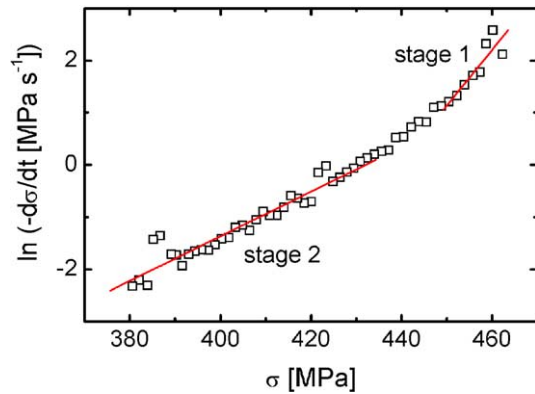


Fig. 6. Stress relaxation curve of F10AZ with inverse curvature taken at 500 °C.

relaxation (strain) rates (stage 1) and a flat one with a higher r at low relaxation rates (stage 2). The r values in the two stages are denoted by r_{rel1} and r_{rel2} .

Average values of the strain rate sensitivity from relaxation tests are collected in Fig. 7 as a function of temperature. The initial values r_{rel1} (large symbols) are small at room temperature and even smaller at 350 °C. At higher temperatures, they show a maximum between about 400 and 700 °C. The values at the maximum are higher for F20A and F20AZ containing 20 at.% Al than those for F10A and F10AZ with 10 at.% Al. Inversely curved relaxation curves do not occur for F10A, but do occur for all other materials in the range of the maximum of r_{rel1} , indicated by the high values of the strain rate sensitivity r_{rel2} in stage 2 (small symbols). The stress exponents m' , calculated from r_{rel1} and σ of individual relaxation tests, are plotted in Fig. 8. These values always coincide for the materials with equal Al content independent of the Zr concentration. They are very high at 350 °C and decrease gradually with increasing temperature down to

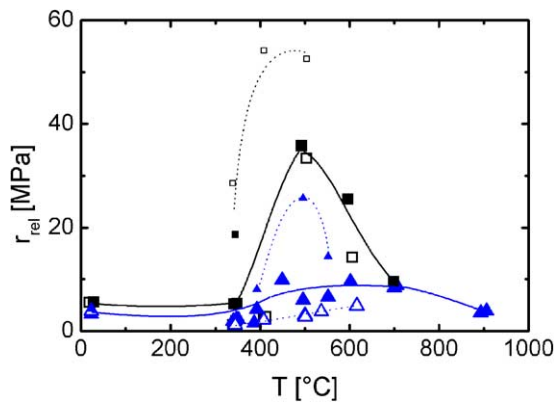


Fig. 7. Average values of the strain rate sensitivity measured by stress relaxation tests as a function of temperature for F10A (open triangles), F10AZ (solid triangles), F20A (open squares), and F20AZ (solid squares). Strain rate sensitivity r_{rel1} in stage 1 of the relaxation curves corresponding to the strain rate prior to the relaxation test (large symbols), strain rate sensitivity in stage 2 r_{rel2} corresponding to lower strain rates (small symbols).

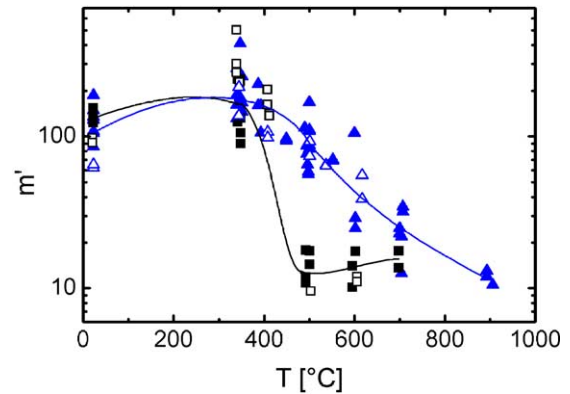


Fig. 8. Stress exponent m' calculated from r_{rel1} and σ of individual stress relaxation curves. Symbols as in Fig. 4.

values between 10 and 20 for the materials with 10 at.% Al and rapidly for those with 20 at.% Al.

Data from the strain rate cycling tests are collected in Fig. 9. As anticipated, the instantaneous strain rate sensitivity r_i of Fig. 9(a) does not differ much from the relaxation data r_{rel} in Fig. 7. The steady state values in Fig. 9(b) are lower and even become negative for the materials without Zr at 350 and 400 °C.

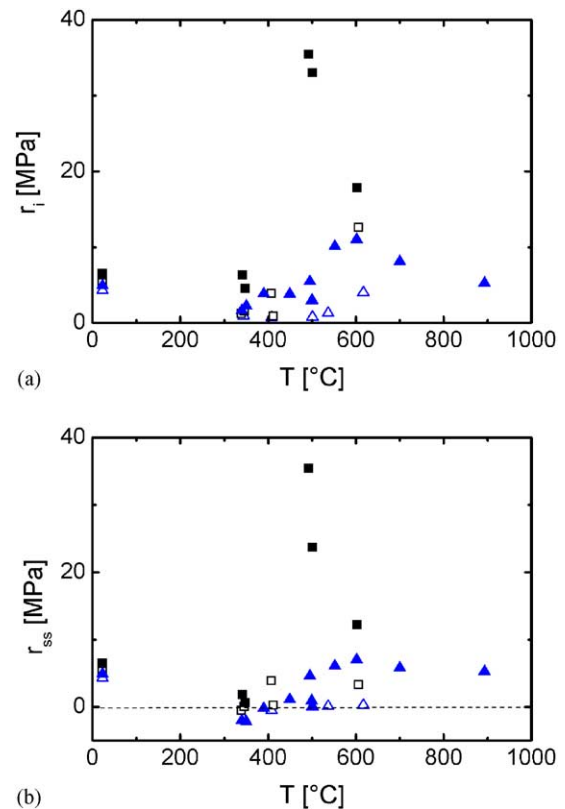
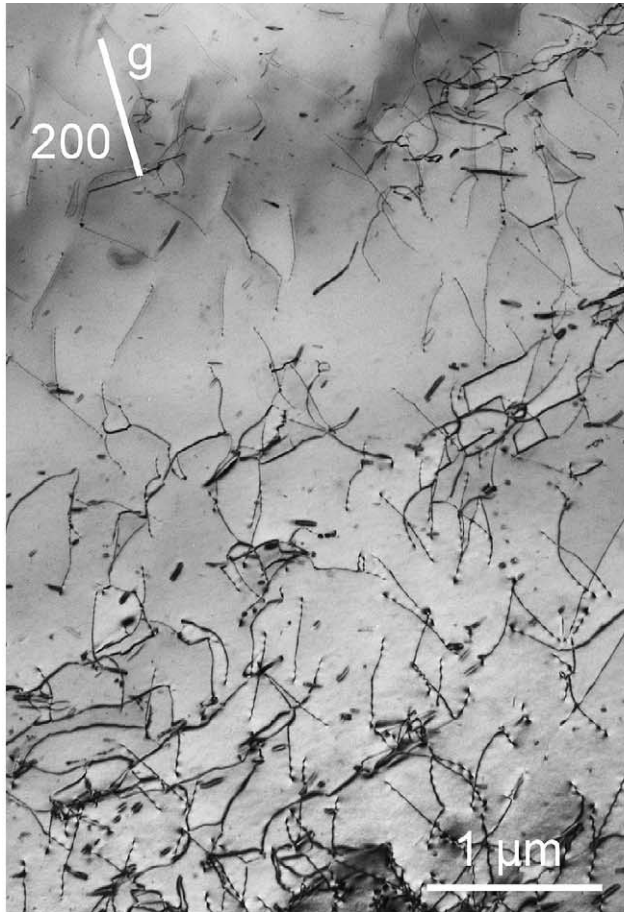
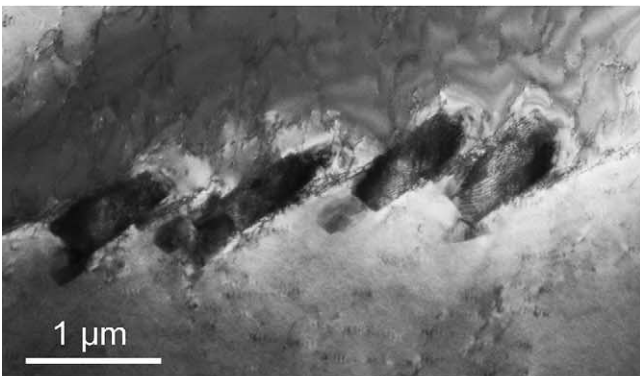


Fig. 9. Average values of the strain rate sensitivity from strain rate cycling tests. (a) Initial strain rate sensitivity r_i . (b) Steady state strain rate sensitivity r_{ss} .

The reference alloy Fe-30Zr, consisting mostly of the Fe₂Zr Laves phase, is brittle up to 600 °C with a fracture stress around 900 MPa. At about 800 °C, the flow stress is around 800 MPa with a strain rate sensitivity $r_{rel} \cong 30$ MPa.



(a)



(b)

Fig. 10. TEM images of the microstructure of the alloy F10AZ deformed at room temperature to a plastic strain of $\varepsilon = 2\%$. (a) Dislocation structure inside a matrix grain. (b) Boundary structure created between two FeAl grains in a gap of the Laves phase precipitate layer.

3.2. Microstructure after deformation at room temperature

Fig. 10(a) shows the dislocation structure inside the grains of the alloy F10AZ after compression at room temperature up to a plastic strain of $\varepsilon = 2\%$. The deformation takes place by slip of ordinary dislocations with $a/2\langle 111 \rangle$ Burgers vectors, which are typical for the disordered b.c.c structure of the Fe-Al matrix. The dislocations are quite homogeneously distributed with an average density of $\rho = 2.7 \times 10^{13} \text{ m}^{-2}$. All dislocation density data are collected in Fig. 11. The dislocation densities are always determined inside the grains and, if slip is localized, inside the slip bands. Comparison of the dislocation structures with projections of the slip planes onto the image plane under different orientations showed that slip takes place on $\{110\}$ and $\{112\}$ planes. The dislocation lines are either crystallographically oriented or smoothly bent. The grain boundaries are usually covered by precipitated Laves phase with relatively frequent interruptions, i.e. gaps where the Fe-Al grains meet each other [7]. In such gaps deformation-induced boundary structures form, as presented in Fig. 10(b).

Fig. 12 presents the microstructure of a F20AZ specimen after a deformation of 2% at room temperature. Inside the grains, the dislocations are inhomogeneously distributed and concentrated in slip bands, as demonstrated in Fig. 12(a). Some dislocations pile up at the grain boundary in the gaps of the grain boundary layers. The dislocation density inside the bands is about $2 \times 10^{13} \text{ m}^{-2}$, in some grains above 10^{14} m^{-2} , in others very low. There occurs a number of dislocation segments which are bent to small radii of curvature. The SEM image in Fig. 12(b) of the surface shows a relief indicating a concentration of deformation inside the soft grains. Microcracks are occasionally formed along the phase boundary and within the grain boundary eutectic (arrows). In the section of the grain boundary layer of Fig. 12(c), some contrasts of dislocations are visible in the Fe-Al lamellae indicating their plastic deformation. This may cause the cracks in the Laves phase. However, these cracks are not very frequent so that the grain boundary layers remain mostly intact.

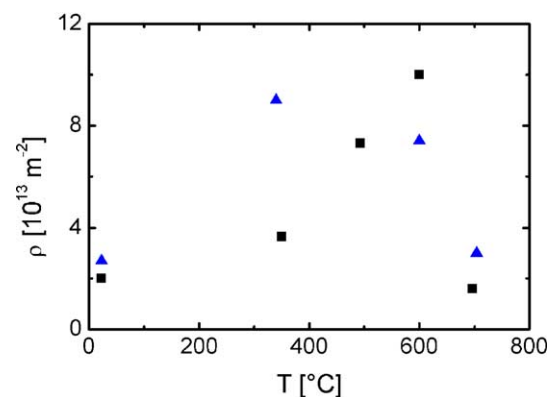


Fig. 11. Dependence of the dislocation density after plastic deformation to about $\varepsilon = 2\%$ on the temperature. Symbols as in Fig. 4.

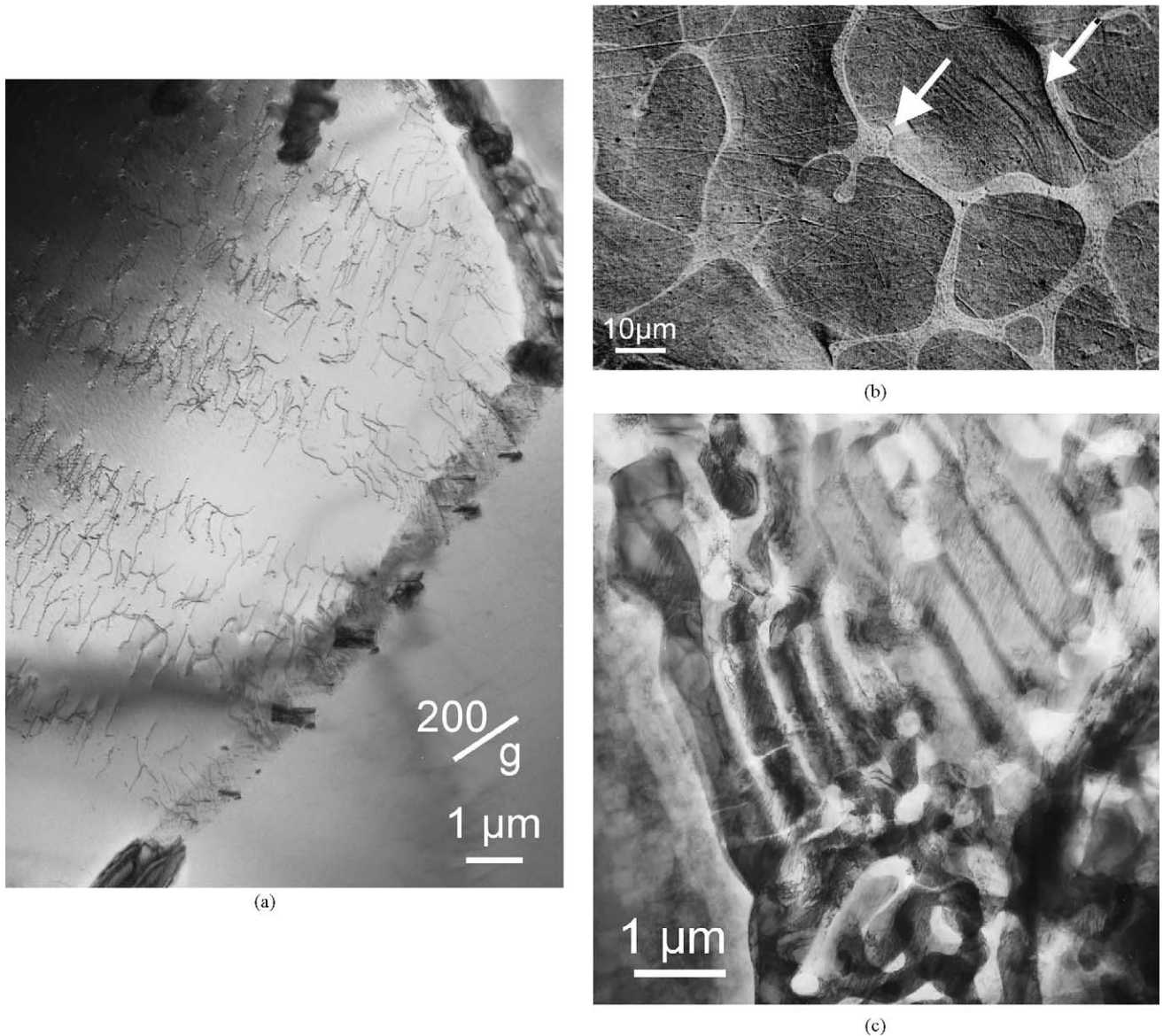


Fig. 12. Microstructure of the alloy F20AZ deformed at room temperature. (a) TEM image showing an inhomogeneous distribution of dislocations in slip bands. (b) SEM image of the surface relief (secondary electron contrast at 5 kV). Arrows indicate cracks. (c) TEM image of a section of the grain boundary phase with dislocations in the Fe-Al channels and cracks of the Laves phase lamellae.

3.3. Microstructure after deformation at intermediate temperatures

Fig. 13(a) presents an overview of the microstructure of the alloy F10AZ after compression at intermediate temperatures. Inside the matrix grains, the dislocations are quite uniformly distributed with a density in the order of 10^{14} m^{-2} (Fig. 13(b)). As in the case of room temperature testing, the dislocations are partly straight and crystallographically oriented. The eutectic is shown in Fig. 13(c) at a higher magnification. Strong contrasts in the Fe-Al channels indicate that there is a high dislocation density in these regions originating from plastic deformation. As shown in Fig. 14(a) for F20AZ, homogeneously distributed dislocations are all curved. Otherwise, the situation is similar to F10AZ. The

grain boundary eutectic again contains Fe-Al regions with many dislocations. In both alloys, the grain boundary eutectic sometimes broke into small blocks, as illustrated in Fig. 14(b). At the grain boundaries, in the gaps of the grain boundary layers, the strains are accommodated by dislocation networks with well developed ledges (Fig. 14(c)). At about 500°C , the wavy shape of the edges of the grain boundary layers indicates heavy deformation in these regions in connection with strain contrasts in the Fe-Al matrix phase (Fig. 14(d)).

3.4. Microstructure at and above 600°C

After deformation at 600°C , the deformation microstructures of the alloys F10AZ and F20AZ reveal similar

dislocation structures shown in Fig. 15 for F10AZ. In Fig. 15(a), bending contours in the matrix indicate inhomogeneous deformation with residual elastic strains. The inset in Fig. 15(a) shows a diffraction pattern of the eutectic grain boundary phase. Diffraction spots of the Laves phase are arranged in rows approximately perpendicular to the boundaries of the lamellae. The individual spots originate from mutually rotated lamellae. The long axes of the spikes of the lamellae, which are approximately perpendicular to the lamellae boundaries, are slightly inclined with respect to the image plane. Thus, the Ewald sphere intersects the spikes of lamellae of different orientations at different places. These misoriented lamellae were not observed in the undeformed material and indicate the deformation of the grain boundary phase. In the gaps of the latter, boundary structures as shown in Fig. 15(b) form, which are similar to those formed at room temperature (Fig. 10(b)). The dislocation density amounts to $7.4 \times 10^{13} \text{ m}^{-2}$.

The tendency to form subgrains within the Fe-Al matrix grains was first observed after deformation at 700 °C. In the alloy F10AZ presented in Fig. 16(a), many cracks separate

grain boundary phase sections about 2 μm in size, leading to strains in the neighbouring matrix regions. The dislocations are distributed very inhomogeneously. The average density is quite low but in some regions the mean density is above 10^{15} m^{-2} . The grain boundary phase is heavily deformed (Fig. 16(b)) as well. In the alloy F20AZ, cracks of the grain boundary phase were not observed but a well developed subgrain structure in the matrix, as demonstrated in Fig. 17. The dislocation density within subgrains is generally low under these conditions.

The dislocation density data in Fig. 11 collected from all specimens show that the density inside the grains increases up to 600 °C and then decreases drastically.

3.5. Dislocation motion during in situ heating in the HVTEM

One specimen was deformed inside the HVTEM. There was intensive dislocation motion at 600–800 °C. Similar observations were made during in situ heating experiments with the alloy F20AZ. At 650 °C, the creation of dislocations and their intensive motion was recorded on video tape

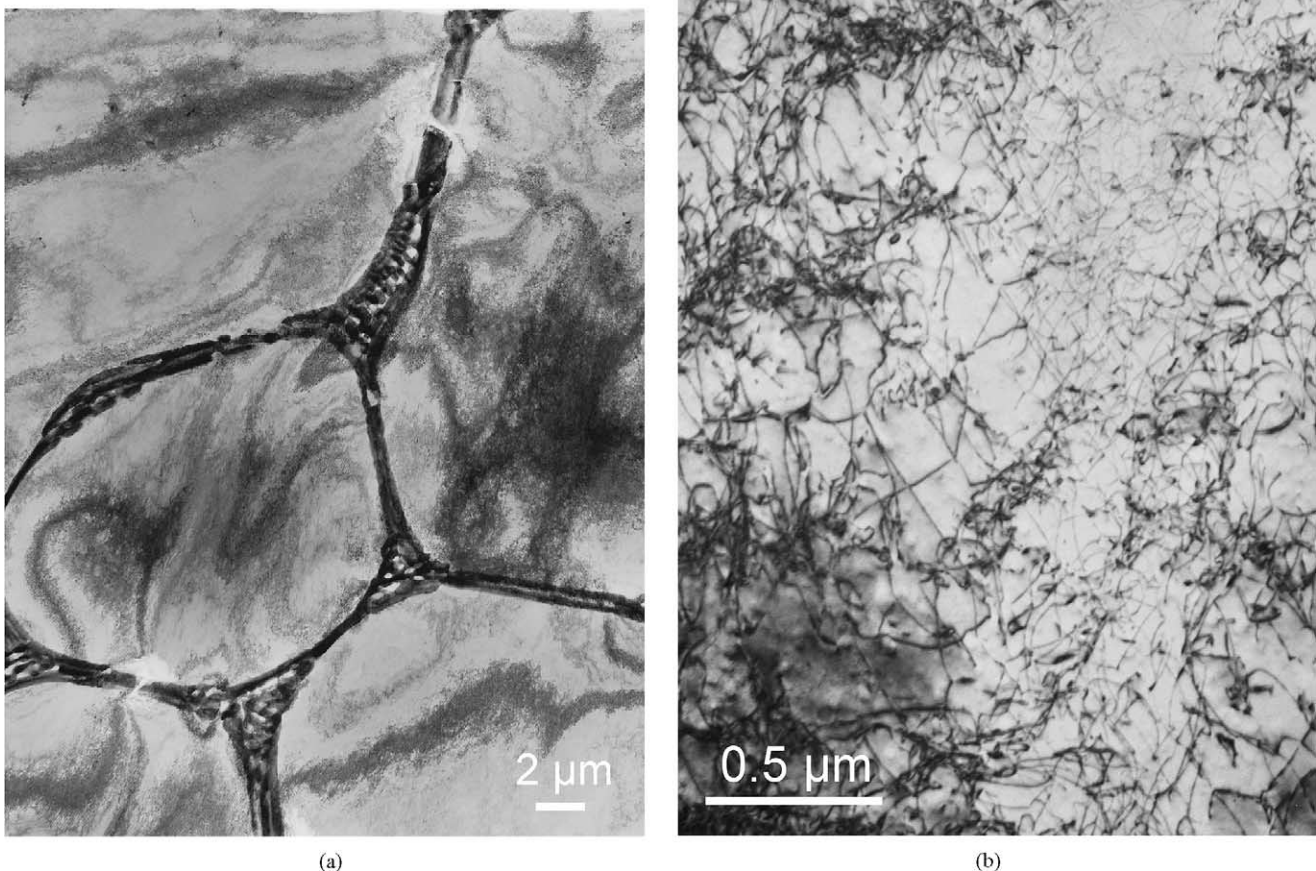


Fig. 13. TEM images of F10AZ after deformation. (a) and (b) 5.7% at different temperatures between 347 and 552 °C and (c) 2% at 340 °C.



(c)

Fig. 13. (Continued).

during a total time of 3 h. Fig. 18(a) shows slip traces left behind by the moving dislocations on the foil surfaces. This image was taken after cooling down to 400 °C where the dislocations seized to move. Slip traces are curved and arranged in very different directions across the Fe–Al grain. The dislocations change their slip plane many times, indicating cross slip and climb. Besides, the video recordings show slip occurring along the boundary of the eutectic phase. In Fig. 18(b), dislocations pile up against the boundary phase after leaving their slip planes.

4. Discussion

Below, the different contributions to the flow stress of the materials are estimated, first those of the matrix grains followed by the strengthening effect of the grain boundary phase. Finally, the high-temperature decrease of the flow stress is discussed.

4.1. Solution hardening

As studied by several authors (for reviews see [10,11]), the addition of aluminium to iron causes a remarkable in-

crease of the flow stress via solution hardening. In pure b.c.c. materials, the dislocation mobility is usually controlled by the Peierls mechanism operating particularly on screw dislocations. As a consequence, the dislocations are arranged mainly along the screw orientation. Some crystallographic orientation of the dislocations was also observed in the present study in F10AZ (Figs. 10 and 13(b)) while the dislocations are curved in F20AZ (Fig. 12(a) and 14(a)), in agreement with the general observation that alloying suppresses the characteristic features of pure b.c.c. materials [11]. The solution hardening in these materials is usually interpreted by the Suzuki effect [12]. The original system of non-linear equations has been approximated in [13]. The theory considers the influence of foreign atoms on the dislocation core energy and thus on the formation of kink pairs. The interaction is described by an interaction energy

$$E_w = \frac{0.122 \text{ eV}(1.52\delta + \eta')\mu}{\mu_0}. \quad (1)$$

δ is a size misfit parameter with $\delta = (1/a)(da/dc)$, where a is the lattice constant and c the atomic fraction of the solute. η' is given by

$$\eta' = \frac{\eta + 4.3\delta}{1 - 1/2(\eta + 4.3\delta)}. \quad (2)$$

η is a modulus misfit parameter defined by $\eta = (1/\mu)(d\mu/dc)$. μ is the shear modulus and μ_0 the value at room temperature. With $\delta = 0.063$ and $\eta = -1.39$ from [12] for Al in Fe, the interaction energy becomes $|E_w| = 0.072 \text{ eV}$. The most prominent feature of the Suzuki theory is the proportionality between the increase in the (shear) flow stress τ_s and the concentration c . A specific calculation for Al in Fe does not exist. From data for Mo and Si in Fe, taken from [13] and listed in Table 2, it can be extrapolated that $d\tau_s/dc = 1.37 \text{ GPa}$ for Al. Since the flow stress contribution τ_s is a shear stress, it has to be multiplied by the Taylor factor M to obtain the contribution σ_s of solution hardening to the macroscopic flow stress. For b.c.c. metals, Taylor factors as low as 1.67 are quoted in the literature. However, $M = 3.06$

Table 2

Theoretical values of the flow stress contributions of the matrix at room temperature.

A			
Material	E_w [eV]	$d\tau/dc$ [GPa]	$(d\tau/dc)/E_w$ [GPa eV ⁻¹]
Mo	0.083	1.57	18.92
Si	0.108	2.01	18.61
Al	0.072	1.37 ^a	19.06 ^a
B			
	σ_s [MPa]	σ_i [MPa]	σ_{HP} [MPa]
F10AZ	420	80	90
F20AZ	840	58	87

(A) Parameters of solution hardening in different Fe alloys. (B) Flow stress contributions from solution hardening, long-range internal stresses and grain structure.

^a Extrapolated.

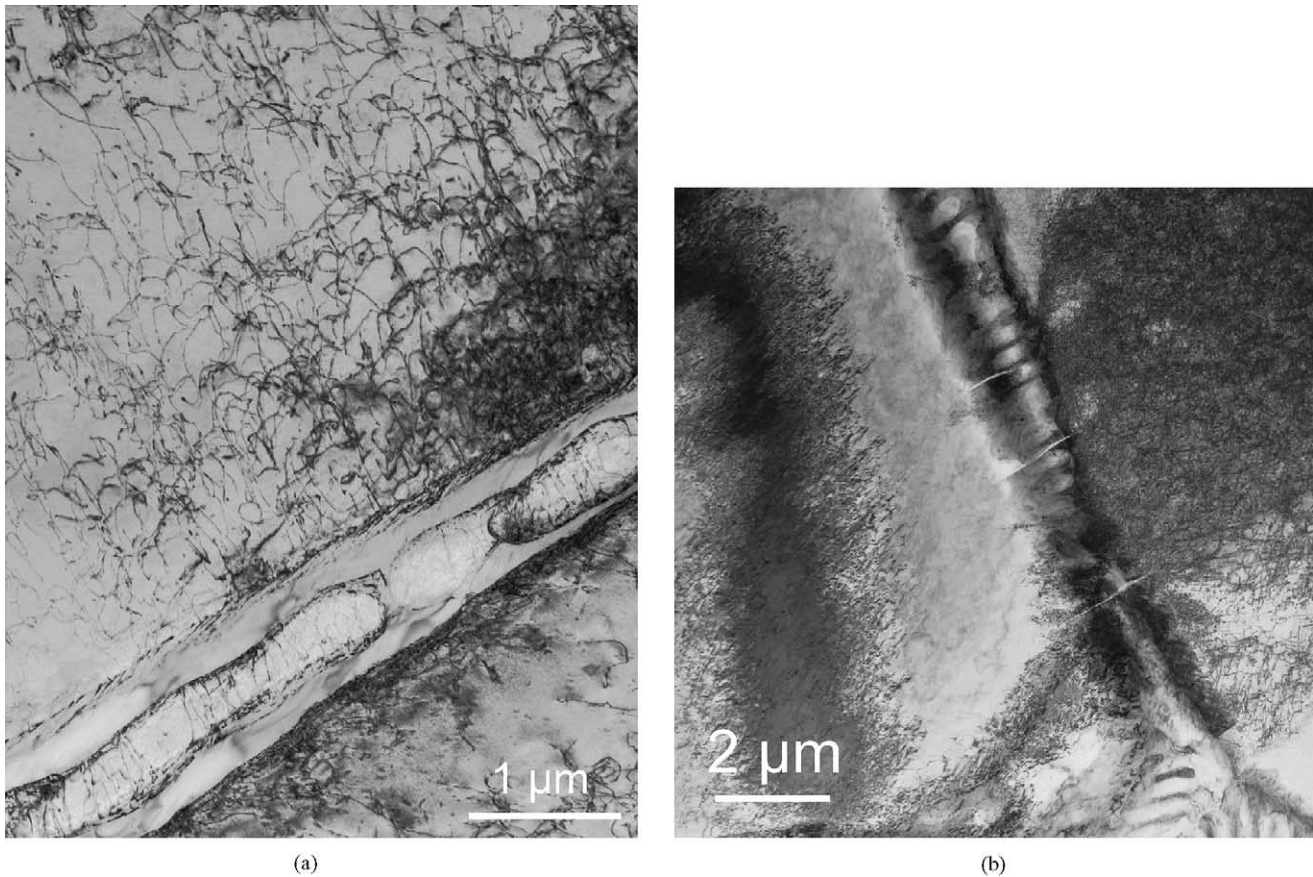


Fig. 14. TEM images of the alloy F20AZ after 2% deformation. (a) Dislocation structure inside grain and in Fe-Al lamella in the grain boundary phase, 349 °C. (b) Cracks in the grain boundary phase, 349 °C. (c) Dislocation networks in the gaps of the grain boundary phase, 349 °C. (d) Wavy interface between grain boundary phase and matrix, 493 °C.

(e.g. [14]) should be a suitable Taylor factor, from which the theoretical values of σ_s at room temperature follow ($\mu = \mu_0$ in Eq. (1)), as listed in Table 2B for the materials F10AZ and F20AZ. These values are about 70% higher than the total flow stresses of the reference materials F10A and F20A without Zr of Fig. 4. Thus, the theory considerably overestimates the solution hardening of Al in Fe. This may, at least partly, result from the large Taylor factor. In the concentration range of the present materials, Fe-Al alloys may show both short and long range ordering [15–18]. Although the state of order in the matrix phase is not clear [7], ordering should not yield a remarkable flow stress contribution.

Calculations of the temperature and strain rate dependence of the flow stress of Fe-Al alloys do not exist, only for Fe-P [19]. This theory predicts a strong temperature dependence in the range from -100 to 100 °C in agreement with experiments. A similar temperature dependence may also be expected for Fe-Al, so that solution hardening cannot explain the almost constant flow stress of most present materials up to 400 °C (Fig. 4). For the activation volume V , which represents the strain rate sensitivity r via

$$V_{\text{ex}} = \frac{MkT}{r} \quad (3)$$

again only calculations for Fe-P are available [19]. They are in the range of $25-200b^3$, where b is the absolute value of the Burgers vector, and decrease with increasing content of the alloying element and decreasing temperature. The experimental values for V/b^3 from Fig. 7 for room temperature are 210 for F10A, 147 for F20A, 240 for F10AZ and 145 for F20AZ. Thus, the present values are roughly in this order of magnitude, they follow the theoretical trends (see also Fig. 7 for the temperature dependence of r) and they are almost equal for the same Al concentrations independent of the addition of Zr. This indicates that the thermally activated deformation occurs predominantly in the matrix grains.

4.2. Diffusion processes in the dislocation cores

In the process of solution hardening, the obstacles are supposed to be locally fixed in the time scale of the dislocation motion. At higher temperatures, the solutes may diffuse in the stress field of the dislocations, giving rise to a Cottrell effect type interaction [20] which is also called dynamic strain ageing. This interaction causes a temperature and strain rate dependent contribution to the flow stress τ_C

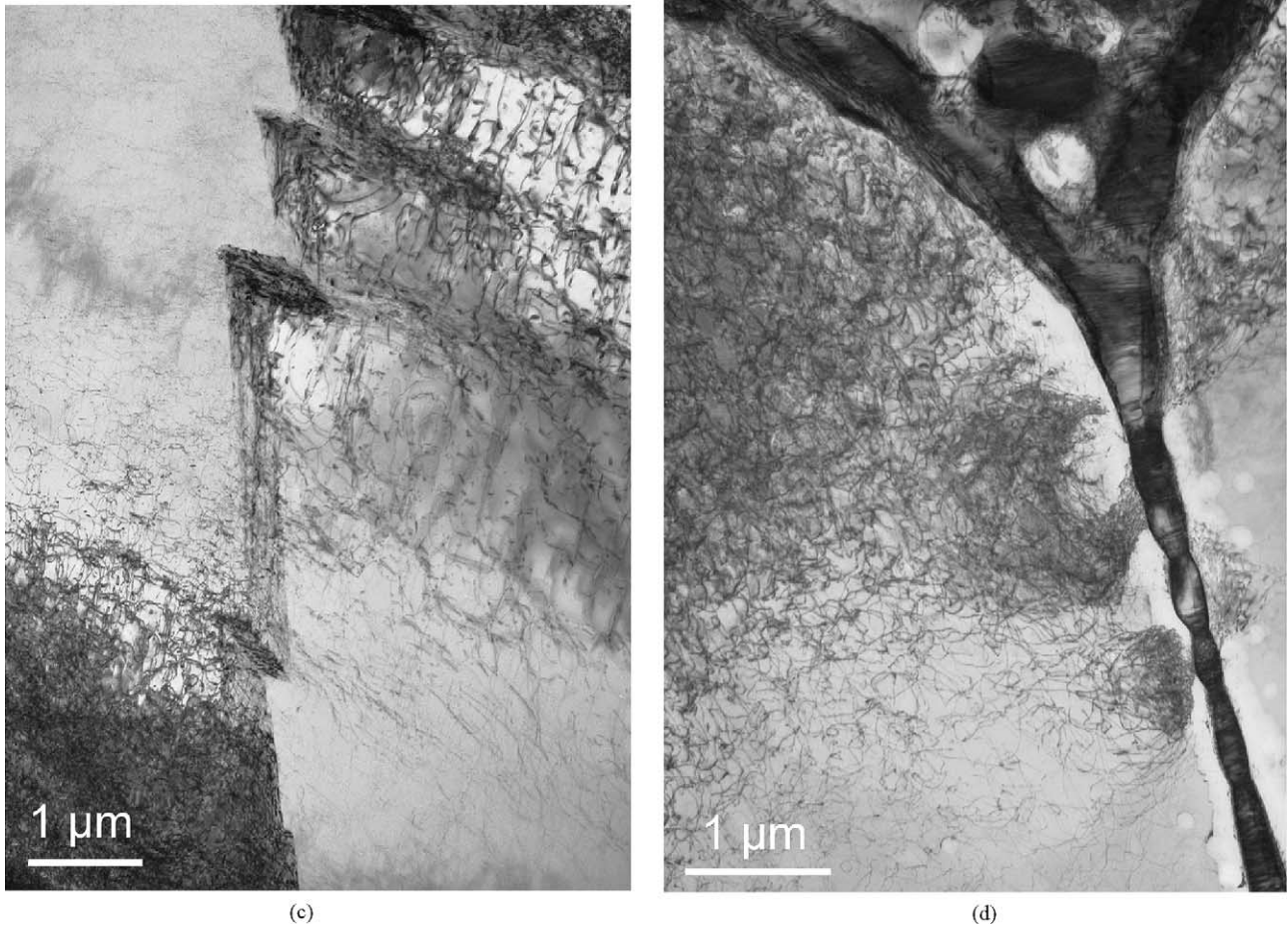


Fig. 14. (Continued).

with a maximum [21]

$$\tau_{\text{Cm}} \cong \frac{17c\beta}{b^4}, \quad (4)$$

where $\beta = (\mu b/3\pi) \{(1 + \nu)/(1 - \nu)\} (\nu_s - \nu_m)$. Here, c is the atomic fraction of the solute and μ is again the shear modulus, which in this paper is always set equal to the energy factor K_s of screw dislocations. K_s was calculated with a computer program [22] based on anisotropic elasticity theory using elastic constants from [23] for Al concentrations of 9.65 and 19.83 at.%. The concentration of Al in the grains is approximately equal to the total concentration in the materials. The resulting values of K_s are 40.64 and 33.44 GPa for the materials with 10 and 20% Al. ν is the Poisson ratio which is set to 0.291, i.e. the Voigt average for Fe [21]. ν_s is the atomic volume of the solute atoms and ν_m that of the matrix atoms. These volumes are calculated assuming spheres with the atomic radii of 0.143 nm for Al and 0.126 nm for Fe [24]. It is supposed that the Cottrell type interaction compensates for the decrease of the solution hardening with increasing temperature. With the data discussed above, τ_{Cm} amounts to about 1.1 GPa for the materials with 10 at.% Al. Thus, much smaller solute concentrations are sufficient

to compensate for the flow stress decrease of solution hardening. At a certain temperature T , the maximum value τ_{Cm} is found at a dislocation velocity

$$v_{\text{dm}} = \frac{4DkT}{\beta}. \quad (5)$$

D is the diffusion coefficient of the diffusing species. Using the Orowan relation between the plastic strain rate $\dot{\epsilon}$ and the dislocation velocity

$$\dot{\epsilon} = \rho b v_d, \quad (6)$$

the diffusion coefficient necessary to obtain the maximum at a certain temperature can be calculated. In order to keep the flow stress of the materials with 10 at.% Al on a high level up to 600 °C, the maximum should be at about 450 °C. With $\dot{\epsilon} = 10^{-4} \text{ s}^{-1}$ and $\rho = 8 \times 10^{13} \text{ m}^{-2}$ from Fig. 11, it follows that $D \cong 3 \times 10^{-19} \text{ m}^2 \text{ s}^{-1}$. Diffusion data for Al in Fe-Al alloys with the present Al concentrations are not available. In Fe-18 at.% Al, diffusion of Fe reaches this value at about 540 °C [25]. Diffusion of Al in the intermetallic compounds in the Fe-Al system was simulated by the diffusion of In and Zn [26] because an appropriate and inexpensive radio-tracer for Al is not available. The diffusion

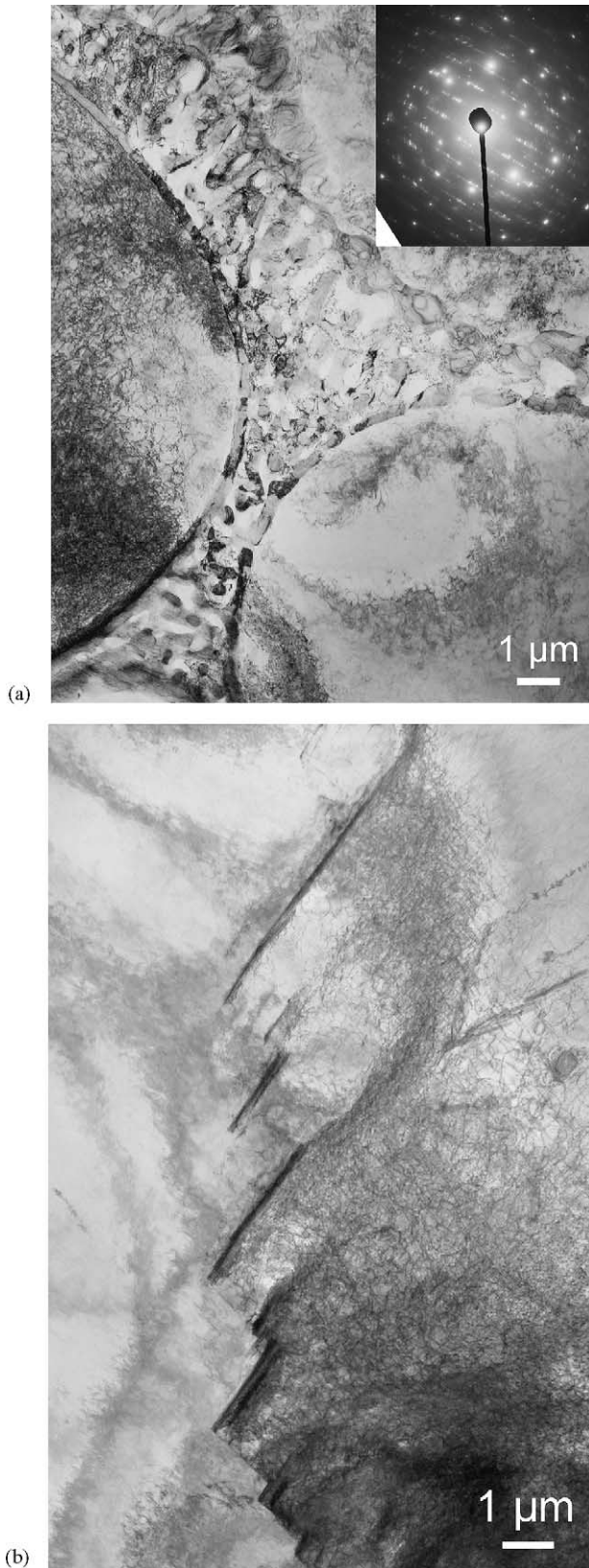


Fig. 15. Microstructure of the alloy F10AZ after deformation at 600 °C. (a) Overview. Inset: diffraction pattern of the grain boundary phase in the centre of the figure. (b) Structure within the gaps of the grain boundary phase.

coefficients in Fe-25.5 at.% Al at the lowest temperature of 450 °C correspond well with the value estimated above.

The contribution of Cottrell effect type interactions to the flow stress has implications on the strain rate sensitivity, as described for intermetallic alloys in [27]. If τ_C is plotted versus the logarithm of the strain rate $\dot{\epsilon}$, the slope of this plot represents the strain rate sensitivity r . At strain rates lower than that for the maximum stress τ_{Cm} , the strain rate sensitivity is positive, but decreases with increasing $\dot{\epsilon}$ down to zero at the maximum. This behaviour is inverse to that of dislocation-obstacle mechanisms. Above the maximum, r even becomes negative. The inverse behaviour is observed in the curvature of stress relaxation curves, e.g. Fig. 6 taken at 500 °C, where the strain rate sensitivity equals the reciprocal slope of the relaxation curve. It increases with decreasing stress in an unusual manner. The occurrence of such higher values of r at the end of the relaxation curves is indicated in Fig. 7 by small symbols. This effect is clearly observed between 350 and 500 °C for F20A, between 400 and 550 °C for F10AZ, and only at 350 °C for F20AZ. Thus, diffusion is apparently more rapid in F20AZ than in F10AZ, which shifts the maximum to lower temperatures resulting in an earlier flow stress decrease of F20AZ at high temperatures, as demonstrated in Figs. 4 and 7. Negative values of the strain rate sensitivity cannot be observed in stress relaxation tests. However, they occur in some cases at 350 and 400 °C in the steady state values r_{ss} measured in strain rate cycling tests, as plotted in Fig. 9(b). This supports the conclusions drawn from the stress relaxation tests.

In conclusion, the Cottrell effect may give rise to a flow stress contribution with a maximum at about 450 °C in F10AZ and at about 350 °C in F20AZ. This contribution compensates for the normal flow stress decrease of solution hardening, especially in the materials with 10 at.% Al, but it is not strong enough to cause a flow stress anomaly.

4.3. Long-range interactions between dislocations

Long-range elastic interactions between dislocations result in an athermal contribution to the flow stress. For a relatively homogeneous arrangement of dislocations, as it was mostly observed in the present study, this contribution can be described by Taylor hardening [28]

$$\sigma_i = \alpha M \mu b \rho^{1/2}, \quad (7)$$

where α is a factor between 0.2 and 1. Taking a typical value of $\alpha = 0.5$ and, as above, K_s instead of the shear modulus μ , the dislocation densities ρ of Fig. 11 lead to athermal stress components in the order of about 100 MPa for temperatures up to 600 °C. The room temperature values are also included in Table 2. No dislocation density data are available for the reference materials F10A and F20A, but it may be assumed that they are similar to those of the materials containing Zr. The increased dislocation densities at intermediate temperatures result from work-hardening in this temperature range so that these values are not characteristic of the yield stress.

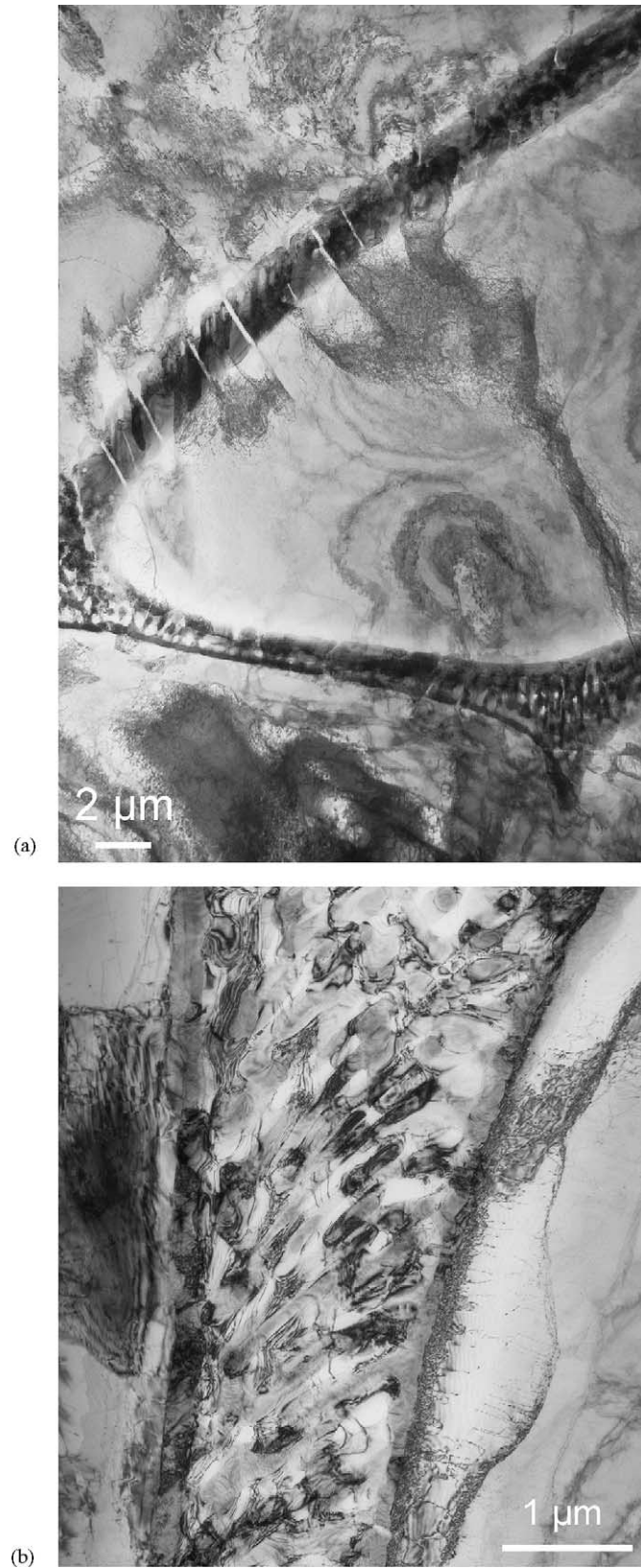


Fig. 16. Microstructure in F10AZ deformed at 698 °C to a plastic strain of $\varepsilon = 2.2\%$. (a) Overview. (b) Structure of deformed grain boundary phase and neighbouring matrix.

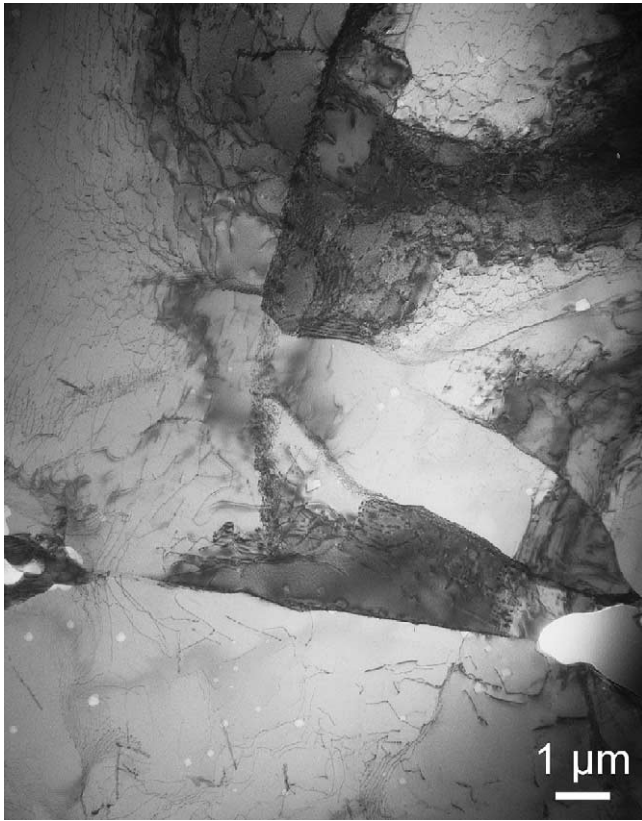


Fig. 17. Subgrain structure in the alloy F20AZ deformed at 704 °C to a plastic strain of $\varepsilon = 3\%$.

The estimation shows that σ_i of the matrix grains is not an essential contribution to the flow stress.

4.4. Influence of the grain structure

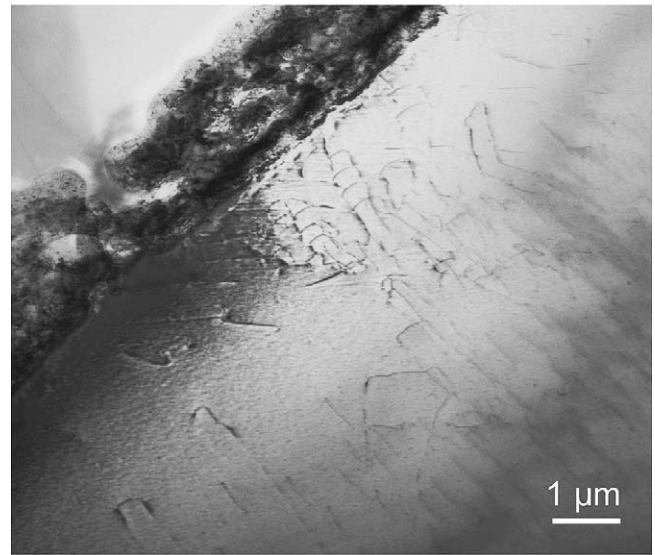
The polycrystalline structure of the materials causes an additional component of the flow stress which can be estimated by the Hall–Petch relation (e.g. [31])

$$\sigma_{\text{HP}} = \gamma_{\text{HP}} M \mu \left(\frac{b}{\bar{D}} \right)^{1/2}, \quad (8)$$

with \bar{D} denoting the grain size and γ_{HP} a factor between 0.06 and 0.18, depending on the details of the mechanism. For the present case where the grain boundaries are reinforced by a hard grain boundary eutectic, $\gamma_{\text{HP}} = 0.18$ should be appropriate. The values for σ_{HP} resulting from the grain sizes of 28 and 20 μm for F10AZ and F20AZ from Table 1 are listed in Table 2B. For the reference materials without Zr, σ_{HP} is negligible since the grain sizes are almost in the millimeter range. Thus, the Hall–Petch component explains the flow stress difference between the materials without and with Zr at least partly. It depends only weakly on the temperature owing to the temperature dependence of the elastic constants.



(a)



(b)

Fig. 18. The microstructure of alloy F20AZ recorded by in situ cooling to 400 °C.

4.5. Contribution of the grain boundary phase

The grain boundary phase consists of a eutectic between the Laves phase and an Fe–Al phase with a lamellar structure. As described at the end of Section 3.1, the Laves phase itself is brittle almost in the whole temperature range of the present study with a fracture stress of about 900 MPa. However, it is embedded in the softer Fe–Al phase. The formation of cracks in connection with the grain boundary eutectic was only occasionally observed at room temperature (e.g. in F20AZ in the SEM image of Fig. 12(b) and within the Laves phase in Fig. 12(c)) and as a decomposition of the grain boundary layers into blocks about 2 μm in size at 350 and 700 °C (Figs. 14(b) and 16(a)). Thus, the grain boundary eutectic remains mostly intact up to 600 °C. However, the occurrence of dislocation structures within the Fe–Al phase (Fig. 10(c), 13(c) and 14(a)), the serrated shape of the inter-

face of the grain boundary layers and the matrix (Fig. 14(c)) and the mutual tilting of Laves phase lamellae (Fig. 15(a)) demonstrate that the Fe-Al phase deforms heavily. The flow stress σ_{GB} of the Fe-Al component of the grain boundary phase may be dominated by a Hall–Petch contribution of the Fe-Al lamellae if the width d of the lamellae is used in Eq. (8) instead of the grain size \bar{D} . With the values for d from Table 1, σ_{GB} is about 1000 MPa for both F10AZ and F20AZ. Accordingly, the stress which builds up in the Fe-Al lamellae is roughly equal to the fracture stress of the Laves phase lamellae so that the latter sometimes break, but not very frequently. If it is taken into account that the Laves phase mostly does not break, $\sigma_{GB} \cong 800$ MPa is a reasonable estimate.

The materials F10AZ and F20AZ represent composites consisting of a soft matrix embedded in a grain boundary skeleton with a much higher flow stress. A theory which considers this morphology is not available. In a very simplified approach, it may be assumed that the matrix and grain boundary phases are deformed up to equal strains so that the flow stress σ_C of the composite is given by a rule of mixture (e.g. [29,30])

$$\sigma_C = (1 - f_{GB})\sigma_M + f_{GB}\sigma_{GB}, \quad (9)$$

where f_{GB} is the volume fraction of the grain boundary phase and σ_M and σ_{GB} are the individual flow stresses of the matrix grains and the grain boundary phase. It may be assumed that

$$\sigma_M = \sigma_s + \sigma_i + \sigma_{HP} \quad (10)$$

from Table 2, where $\sigma_s + \sigma_i$ should be equal to the flow stress σ_R of the reference materials F10A and F20A without Zr from Fig. 4, since the theoretical value of σ_s in Table 2 is too high, therefore

$$\sigma_M = \sigma_R + \sigma_{HP} \quad (11)$$

Using σ_R for about 100 °C from Fig. 4, the volume fractions f_{GB} from Table 1 and a flow stress of the grain boundary phase σ_{GB} estimated above yields the flow stresses of the composites σ_C of about 440 and 645 MPa for F10AZ and F20AZ, respectively. While the latter value of F20AZ fits the experimental value of Fig. 4 very well, the theoretical value is too high for F10AZ. The data estimated in this section refer to temperatures near room temperature. However, all stress contributions except that from solution hardening, σ_s , depend only weakly on temperature. The decrease of σ_s with increasing temperature is compensated by a positive temperature dependence of the contribution of the Cottrell effect, resulting in a stress plateau up to intermediate temperatures.

4.6. Recovery at high temperatures

Above a certain temperature which is about 600 °C for F10AZ and 400 °C for F20AZ, the flow stress decreases strongly. On the one hand, this is due to the fact that both mechanisms involving the solutes, i.e. the solution hardening and the Cottrell effect, cease to operate at these high

temperatures. On the other hand, recovery processes become active at high temperatures. Climb is involved in the recovery processes. The occurrence of climb at high temperatures is apparent from the curved shape of slip traces during the in situ straining and heating experiments (Fig. 18). Climb processes are controlled by self diffusion, which is essentially the diffusion of Fe. In the Fe-Al alloys, Al diffuses more rapidly than Fe, as shown by interdiffusion experiments on Fe-18 at.% Al at 980 °C yielding a factor of 1.8 [31] and by the experiments with the simulation of the Al diffusion by diffusion of In and Zn in Fe₃Al yielding a factor of up to 14 at a lower temperature (450 °C) [26]. This shows that recovery starts at a higher temperature than that of the maximum of dynamic strain ageing. Again, the temperatures are higher for F10AZ than for F20AZ which implies that the diffusion is more rapid in the latter material. Such a behaviour was observed above the Curie temperature (around 700 °C) but the situation is unclear at lower temperatures [25].

The recovery processes are obvious from the formation of a subgrain structure at 700 °C as demonstrated in Fig. 17. Accordingly, the dislocation densities inside the grains, plotted in Fig. 11, have similar values as those at room temperature. The corresponding athermal contributions σ_i to the flow stress are about half of the yield stresses in Fig. 4, i.e. the long-range interaction between the dislocations is an essential contribution to the flow stress. In addition, the strengthening effect of the grain boundary skeleton has disappeared, partly because its Fe-Al component is too soft and partly because the grain boundary eutectic breaks into small blocks by plastic deformation.

Recovery processes also influence the strain rate sensitivity. This can be observed from the temperature dependence of the stress exponent m' in Fig. 8. At 350 °C, it assumes values of several hundred in accordance with the low strain rate sensitivity in the range of dynamic strain ageing. With increasing temperature, m' decreases down to values around 10. According to standard models of recovery-controlled creep, the stress exponent should be between about 3 and 6. The difference between the experimental and theoretical values may be due to some other residual component of the flow stress. In the logarithmic scale of Fig. 8, the decrease is smooth for F10A and F10AZ but rapid above 400 °C for F20A and F20AZ. This is in agreement with the observation that the yield stress also decreases at lower temperatures for the materials with 20% Al compared to those with 10%. Besides, the stress exponents are equal for the materials with the same Al content each, independent of the content of Zr, in accordance with the deformation processes occurring in the soft Fe-Al phase.

5. Conclusions

- Fe-Al alloys with up to 20 at.% Al and an addition of 2.5 at.% Zr, consisting of soft Fe-Al grains embedded in a hard skeleton of a grain boundary eutectic with a Laves

phase component, exhibit a flow stress of about 600 MPa up to about 400 °C and may thus be suited for applications up to this temperature.

- They show strong solution hardening during deformation at room temperature. The decrease of the solution hardening with increasing temperature is compensated by dynamic strain ageing due to a Cottrell effect interaction between dislocations and the Al solutes around 450 °C.
- Long-range elastic interactions between dislocations result in an athermal component of the flow stress which is not important up to about 600 °C. At 700 °C, it is an essential contribution to the flow stress.
- The addition of Zr and its segregation to the grain boundaries leads to a smaller grain size with respect to the reference materials without Zr. This strengthens the materials owing to a Hall–Petch component of the flow stress.
- The grain boundary eutectic deforms inside the Fe–Al lamellae. The flow stress of this phase is mainly controlled by a Hall–Petch component based on the width of the lamellae. The contribution to the total flow stress of the alloys may be estimated by a rule of mixture. The Laves phase lamellae are brittle.
- The high-temperature decrease of the flow stress is partly caused by recovery.

Acknowledgements

The authors wish to thank Rosamunde Möhner and Christian Dietzsch for technical help. Financial support by the Deutsche Forschungsgemeinschaft (DFG) is gratefully acknowledged.

References

- [1] A. Halstead, R.D. Rawlings, *J. Mater. Sci.* 20 (1985) 1248.
- [2] K. Chen, S.M. Allen, J.D. Livingston, *Mat. Res. Soc. Symp. Proc.* 288 (1993) 373.
- [3] D.R. Johnson, *Processing and Mechanical Properties of NiAl-Based In-situ Composites*, PhD Thesis, NASA Contractor Report, University of Tennessee, 1994.
- [4] F. Stein, M. Palm, G. Sauthoff, in: *Proceedings of the Symposium: Werkstoffwoche'98*, vol. VI, Wiley-VCH, Weinheim, Germany, 1998, p. 515.
- [5] F. Stein, G. Sauthoff, M. Palm, *The Fe–Al–Zr system*, private communication, 2003.
- [6] F. Stein, M. Palm, G. Sauthoff, *Struktur und Verformungsverhalten von Fe–Al–Zr-Legierungen mit verstärkenden intermetallischen Phasen für Hochtemperaturanwendungen (Final Report DFG PA 705/3-1)*, 2001.
- [7] A. Wasilkowska, M. Bartsch, F. Stein, M. Palm, K. Sztwiertnia, G. Sauthoff, U. Messerschmidt, Part I of this paper, this issue.
- [8] A. Wasilkowska, M. Bartsch, M. Palm, F. Stein, G. Sauthoff, U. Messerschmidt, in: *Proceedings of the Conference: "20 Years Department of Physical Metallurgy and Materials Technology"*, March 2001, Technical University Gabrovo, Bulgaria, 2001, p. 33.
- [9] C. Schlesier, J.H. Schneibel, R.P. Wahi, *Z. Metall.* 88 (1997) 810.
- [10] K. Vedula, in: J.H. Westbrook, R.L. Fleischer (Eds.), *Intermetallic Compounds*, vol. 2, Wiley, Chichester, 1995, p. 199.
- [11] H. Neuhäuser, C. Schwink, in: H. Mughrabi (Ed.), *Materials Science and Technology*, vol. 6, VCH, Weinheim, Germany, 1993, p. 191.
- [12] H. Suzuki, in: F.R.N. Nabarro (Ed.), *Dislocations in Solids*, vol. 4, North-Holland, Amsterdam, 1979, p. 191.
- [13] H. Hattendorf, A.R. Büchner, *Z. Metall.* 83 (1992) 9.
- [14] R.E. Stoller, S.J. Zinkle, *J. Nuclear Mater.* 283–287 (2000) 349.
- [15] J. Herrmann, *Untersuchungen zur Struktur und zum mechanischen Verhalten von Fe-reichen Fe–Al-Legierungen*, VDI-Verlag, Düsseldorf, 2000.
- [16] J. Herrmann, G. Inden, G. Sauthoff, *Acta Mater.* 51 (2003) 2847.
- [17] J. Herrmann, G. Inden, G. Sauthoff, *Acta Mater.* 51 (2003) 3233.
- [18] G. Frommeyer, E.J. Drewes, B. Engl, *Rev. metall. CIT* (2000) 1245.
- [19] H. Hattendorf, A.R. Büchner, *Z. Metall.* 81 (1990) 739.
- [20] A.H. Cottrell, *Phil. Mag.* 74 (1953) 829.
- [21] J.P. Hirth, J. Lothe, *Theory of Dislocations*, Wiley, New York, 1982.
- [22] D. Baither, *PC programme for dislocation line energy and line tension in anisotropic elasticity*.
- [23] H.J. Leamy, E.D. Gibson, F.X. Kayser, *Acta Metall.* 15 (1967) 1827.
- [24] J. D'Ans, E. Lax, *Taschenbuch für Chemiker und Physiker*, vol. 3, H. Blachnik (Ed.), Springer-Verlag, Berlin, 1998.
- [25] V.S. Raghunathan, B.D. Sharma, *Phil. Mag. A* 43 (1981) 427.
- [26] M. Eggersmann, H. Mehrer, *Phil. Mag. A* 80 (2000) 1219.
- [27] U. Messerschmidt, S. Guder, D. Häussler, M. Bartsch, *Mat. Res. Soc. Symp. Proc.* 652 (2001) Y11.6.1.
- [28] G.J. Taylor, *Proc. Roy. Soc. A* 145 (1934) 362.
- [29] J.G. Sevillano, in: *Materials Science and Technology*, vol. 6, H. Mughrabi (Ed.), VCH, Weinheim, Germany, 1993, p. 19.
- [30] L. Durand, *Mater. Sci. Technol.* 3 (1987) 105.
- [31] M. Weinlagen, B. Köhler, J. Wolff, Th. Hehenkamp, *Defects Diffusion Forum* 143–147 (1997) 449.